A fractional order sliding mode control-based topology to improve the transient stability of wind energy systems

Md Nafiz Musarrat, Afef Fekih [*]

University of Louisiana at Lafayette, P.O. Box 43890, Lafayette, LA, USA

ARTICLE INFO

ABSTRACT

This paper proposes a control topology that integrates the robust performance of fractional order sliding mode control with the high charging/discharging rate and low maintenance requirements of super-capacitors to improve the transient stability of wind energy systems. The observer-based fractional-order sliding mode control (FOSMC) approach is designed to regulate the dc-link voltage and mitigate dynamic instabilities resulting from grid faults, matched and mismatched uncertainties and parameter variations. The super-capacitor, on the other hand, serves as an additional energy storage element that prevents dangerous current surges thereby stabilizing the power delivered to the grid. The proposed approach was validated using a DFIG-based wind energy system installed in a small-scale standalone power supply network. The obtained results confirmed the approach's ability to effectively reduce current fault induced ripples and properly regulate the dc link voltage. They also revealed a remarkable reduction in the thermal stress of semiconductor junctions in the presence of grid faults and disturbances. A further comparison with a standard sliding mode control (SSMC) approach showed that the use of fractional calculus to formulate the FOSMC resulted in smoother control actions and reduced chattering effects compared to SSMC.

1. Introduction

According to the International Renewable Energy Agency, wind is projected to supply more than one-third of the total electricity generation needs by 2050 [1]. The integration of large amounts of wind energy into the grid, however, entails devising proper mechanisms to address the dynamic voltage stability problem and support the grid under faulty operating conditions [2–10]. Additionally, since wind turbines are often remotely installed and costly to maintain and repair, accommodating faults and mitigating their effects in the early occurrence is fundamental to improving their reliability, availability and efficiency. DFIG-based wind turbines account for the majority of deployed wind energy sources. This wide adoption is due to various attributes such as speed variability, low rated inverters, and ability to decouple the control of the active and reactive powers. DFIG-based wind turbines achieve their variable speed operation via two back to back voltage source converters; RSC and GSC. The direct connection of the converters to the grid, however, increases their vulnerability to grid faults or short duration reductions in *rms* voltage that might either be triggered by sudden load fluctuations, short circuits, lightning, or overloading. These faults often

result in a sudden short circuit current in the stator coils. Since this latter is magnetically coupled with the rotor coils, the fault will result in a sudden surge in the rotor currents by as much as two to three-fold its nominal value [7]. These high currents are not acceptable and might result in significant damages to the back to back converters. Further, when faults occur, the drivetrain experiences a highly oscillating torque due to the sudden change in dc-link voltage, thus resulting in a reduction in the reliability of the turbine's shaft. Therefore, devising fast and efficient measures to protect the converters during grid faults is essential in maintaining the dynamic stability of the wind energy system and preventing such faults from causing a widespread loss of power generation.

Active power and voltage support are very important, especially during grid faults. Crowbar is the most popular FRT technique [8]. It protects against grid faults by isolating the RSC from the rotor coil current. However, the sudden activation of the crowbar results in the consumption of a significant amount of reactive power, thus significantly stressing the drivetrain and further worsening the voltage sag condition at the PCC [8–10]. Various alternative strategies to crowbar have been investigated in the literature. The authors in [11] proposed improving the FRT capability of a DFIG-based wind turbine by

---

Nomenclature

WECS	Wind Energy Conversion System
WT	Wind Turbine
DFIG	Doubly Fed Induction Generator
RSC (GSC)	Rotor Side Converter (Grid Side Converter)
FRT	Fault Ride Through
SMC	Sliding Mode Control
TSMC	Terminal Sliding Mode Control
ITSMC	Integrated Terminal Sliding Mode Control
PI	Proportion Integral
FOSMC	Fractional Order Sliding Mode Control
DO	Disturbance Observer
PWM	Pulse Width Modulation
PCC	Point of Common Coupling

P_s (Q_s)	Active (reactive) stator power
P_{dfig} (Q_{dfig})	Total active (reactive) power from DFIG
P_{GSC} (Q_{GSC})	Active (reactive) power from GSC
V_{gsc_d} (V_{gsc_q})	Direct (quadrature) components of the GSC voltage
i_{gd} (i_{gq})	Direct (quadrature) components of the GSC current
i_{rd} (i_{rq})	Direct (quadrature) components of the rotor current
V_{rd} (V_{rq})	Direct (quadrature) components of the rotor voltage.
V_{sd} (V_{sq})	Direct (quadrature) components of the stator voltage
V_{gd} (V_{gq})	Direct (quadrature) components of the grid side voltage
M	Mutual inductance
ψ_{sd} (ψ_{sq})	Direct (quadrature) components of the stator flux
R_s (R_r)	Stator (rotor) resistance
L_s (L_r)	Stator (rotor) inductance
$L_r(R_r)$	Stator (rotor) resistance
$\omega_s(\omega_r)$	Stator (rotor) electric angular pulsation

---

integrating a dc chopper in the dc-link. Reference [12], on the other hand, considered the implementation of series dynamic breaking resistors in the rotor circuit to offset the high rotor current during fault. In [13], a fault current limiter was used to limit the dc-link voltage surge. Other techniques considered integrating an energy storage unit with the dc-link as a spinning reserve [14,15]. Though the integration of the energy storage support resulted in improved recovery time and dc-link voltage regulation under grid faults, those approaches were not able to halt the activation of the crowbar [16]. Several control strategies were proposed in the literature to mitigate dynamic instabilities resulting from grid faults. Linear approaches were the most popular due to their simple design and ease of implementation. However, their lack of robustness to un-modeled dynamics and inherent nonlinearities hampered their efficiency.

A number of nonlinear control approaches have been proposed in the literature to circumvent the above mentioned drawback such as fuzzy logic control [17] model predictive control [18], energy shaping control [19], and sliding mode control (SMC) [20–22] to list a few. Sliding mode control, however, is among the most effective robust control technique for nonlinear systems with uncertainties and external disturbances [23]. Its robustness and inherent suitability for switching-type devices make it especially popular with power electronic converters [24]. However, the chattering phenomena associated with standard SMC can lead to high frequency vibrations that can potentially compromise the dynamic stability and reliability of the wind energy system [25]. To mitigate this problem, linear hyper-planes have been replaced by nonlinear switching manifolds in terminal sliding mode control (TSMC). However, whereas TSMC provides asymptotic stability, it does not guarantee the reachability of the sliding manifold in finite time [26]. Hence, several hybrid sliding mode control techniques such as fuzzy SMC [27], adaptive SMC [28], higher order SMC have been proposed [29–31] to minimize the chattering effect and foster global convergence. However, SMC approaches can only guarantee robust performance for matched disturbances, i.e. those that enter the system via the same channels as the control input, and lose their nominal performance in the presence of mismatched disturbances, i.e. those that enter the system from other channels than the control input [32].

Recently fractional order SMC has emerged as a powerful control design [33]. The application of fractional order calculus provides an extra degree of freedom that facilitates the design of more flexible and powerful control methods that satisfy system specifications [34]. FOSMC designs were shown to exhibit minimal chattering, robust performance against variations in gain, and the ability to reject noise and output disturbances [35]. A FOSMC approach was designed in [36] for a DC buck using switching surfaces based on fractional-order PID and PI structures. An FO-TSMC approach was proposed in [37] to regulate the output voltage of a DC-DC Buck converter. A FOSMC strategy was

proposed in [38] to directly control the active/reactive power output of a DFIG-based wind energy conversion system. Only nominal conditions, however, were considered in the aforementioned approaches and their performance and applicability under faulty grid conditions were overlooked. A robust FOSM controller was proposed in [39] for maximum power point tracking control of DFIG-based wind energy conversion system. A passive fractional-order sliding-mode control (PFOSMC) was proposed in [40] for supercapacitor energy storage (SCES) systems in microgrid with distributed generators. It performance was analyzed using both a simulation study and hardware in the loop implementation, and was shown to improve the system's transient performanmce. An adaptive fractional-order sliding-mode control (AFOSMC) was developed in [41], for superconducting magnetic energy storage (SMES) systems. The proposed approach considered a sliding-mode state and perturbation observer (SMSPO) to estimate the SMES's combined effect of modelling uncertainties, unknown parameters, and external disturbances, then fully compensated for them using a FOSMC approach. A comparison with four other approaches showed that the proposed FOSMC-based framework outperformed the other approaches in terms of tracking speed and cost. Although the above mentioned approaches reported results promising results, major issues associated with improving transient stability such as mitigating the surge in dc-link voltage, loading of GSC, grid frequency are still open research questions.

This paper proposes a fractional order SMC-based (FOSMC) approach to effectively mitigate dynamic instability resulting from grid faults, mismatched uncertainties and parameter variations, whilst providing robust performance to both matched and unmatched disturbances. Its main contributions are threefold:

- A control topology that integrates the robust performance of fractional order sliding mode control with the high charging/discharging rate and low maintenance requirements of super-capacitors to improve the transient stability of wind energy systems.
- A robust SMC approach formulated based on fractional calculus to ensure smooth control actions and alleviate the chattering problem typically associated with standard SMC.
- A design that prevents thermal stress on the converters' semiconductor junctions during grid faults thereby extending the wind energy system's lifespan.

The remainder the paper is structures as follows. Section 2 briefly describes the dynamic model of the DFIG-based wind energy system. Section 3 details the proposed FOSMC-based control topology. Section 4 validates the efficiency of the proposed design and highlights its ability to mitigate the dynamic instabilities resulting from grid faults. Finally, Section 5 concludes the paper.
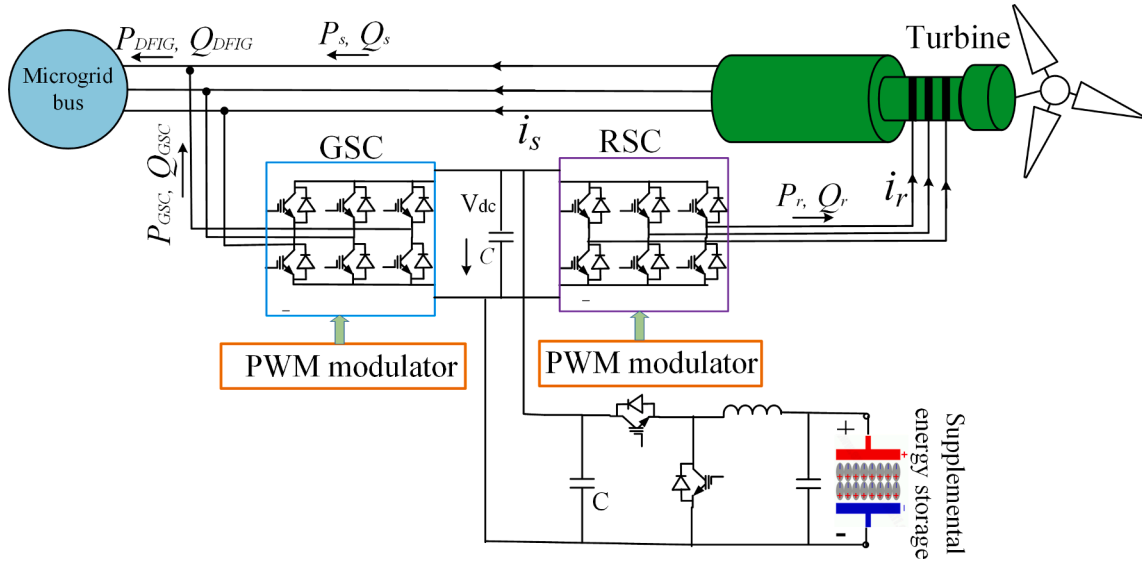
Fig. 1. Schematic diagram of a DFIG-based wind energy system with a supplemental energy storage.

2. System modeling

A general schematic of the grid-connected DFIG-based wind energy system, bidirectional converters and buck boost converter are depicted in Fig. 1.

Here, the main function of the rotor side converter (RSC) is to control the current injected into the rotor coils so that the rotor angular speed follows the set reference. The main function of the grid side converter (GSC) is to regulate the dc-link voltage to near its rated value. The bi-directional buck-boost converter, on the other hand, provides supplemental energy support and improves the regulation of the dc-link voltage.

The mathematical models of the above-described components are briefly introduced below.

2.1. Mathematical modeling of the RSC

Considering $X_R = \begin{bmatrix} i_{r,d} & i_{r,q} \end{bmatrix}^T$ as the state matrix and $\begin{bmatrix} u_{r,d} & u_{r,q} \end{bmatrix}^T = \begin{bmatrix} V_{r,d} & V_{r,q} \end{bmatrix}^T$ as the input matrix, the state space model of a DFIG in a synchronous d-q reference frame, can be modelled as follows [42]:

$$\dot{X}_R = f_1(x,t) + g_1(x,t)u_r \tag{1}$$

With:

$$f_1(x,t) = \begin{bmatrix} \left\{ \begin{aligned} &-\frac{R_r}{(\sigma L_r)^2}\left(\sigma L_r i_{r,d} + \frac{MV_{s,q}}{\omega_s L_s}\right) \\ &+\frac{R_r M \psi_{s,d}}{L_s(\sigma L_r)^2} + \frac{\omega_r}{\sigma L_r}\left(\sigma L_r i_{r,q} + \frac{MV_{s,d}}{\omega_s L_s}\right) \end{aligned} \right\} \\ \left\{ \begin{aligned} &-\frac{R_r}{(\sigma L_r)^2}\left(\sigma L_r i_{r,q} + \frac{MV_{s,d}}{\omega_s L_s}\right) + \\ &\frac{R_r M \psi_{s,q}}{L_s(\sigma L_r)^2} + \frac{\omega_r}{\sigma L_r}\left(\sigma L_r i_{r,d} + \frac{MV_{s,q}}{\omega_s L_s}\right) \end{aligned} \right\} \end{bmatrix}, g_1(x,t)$$

$$= \begin{bmatrix} \frac{1}{\sigma L_r} & 0 \\ 0 & \frac{1}{\sigma L_r} \end{bmatrix}, \tag{2}$$

where, $\sigma = 1 - \frac{M^2}{L_s L_r}$.

If we consider a reference frame synchronously rotating with the

stator flux and neglect the stator resistance, we have:

$$\psi_{s,d} = \psi_s; \psi_{s,q} = 0;\ V_{s,d} = 0 \tag{3}$$

$$V_{s,q} = V_s = \omega_s \psi_s \tag{4}$$

Thus (2) can be re-written as:

$$\dot{X}_R = f_1(x,t) + g_1(x,t)u_r \tag{5}$$

with:

$$f_1(x,t) = \begin{bmatrix} \underbrace{-\frac{R_r}{(\sigma L_r)^2}\left(\sigma L_r i_{r,d} + \frac{MV_s}{\omega_s L_s}\right) + \frac{R_r M \psi_s}{L_s(\sigma L_r)^2} + \omega_r i_{r,q}}_{F_{r,d}} \\ \underbrace{\frac{R_r}{\sigma L_r}i_{r,q} - \frac{\omega_r}{\sigma L_r}\left(\sigma L_r i_{r,d} + \frac{M}{\omega_s L_s}V_{s,q}\right)}_{F_{r,q}} \end{bmatrix}$$

2.2. Mathematical modeling of the GSC

The main function of the GSC is to regulate the voltage across the dc-link and compensate for any fluctuations in the events of active or reactive power variation in the common bus. The dynamic model of the GSC in the synchronous (d-q) reference frame is represented by:

$$\begin{cases} L_g \dfrac{di_{g,d}}{dt} = V_{gd} - V_{gsc,d} - R_g i_{gd} + \omega_s L_g i_{gq} \\ L_g \dfrac{di_{g,q}}{dt} = V_{gq} - V_{gsc,q} - R_g i_{gq} - \omega_s L_g i_{gd} \end{cases} \tag{6}$$

The GSC can be represented by the following state space model:

$$\dot{X}_G = f_2(x,t) + g_2(x,t)u_g \tag{7}$$

where,

$$f_2(x,t) = \begin{bmatrix} \frac{1}{L_g}\left(V_{gd} - R_g i_{gd} + \omega_s L_g i_{gq}\right) \\ \frac{1}{L_g}\left(V_{gq} - R_g i_{gq} - \omega_s L_g i_{gd}\right) \end{bmatrix}, g_2(x,t) = \begin{bmatrix} -\frac{1}{L_g} & 0 \\ 0 & -\frac{1}{L_g} \end{bmatrix} \tag{8}$$

The input vector, $\begin{bmatrix} u_{g,d} & u_{r,q} \end{bmatrix}^T = \begin{bmatrix} V_{gsc,d} & V_{gsc,q} \end{bmatrix}^T$.
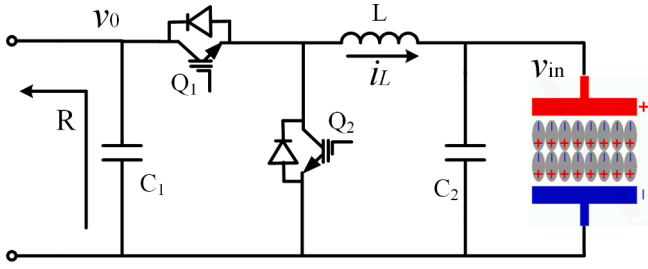
Fig. 2. Schematic of a bi-directional dc/dc converter with a super-capacitor as input voltage source.

2.3. Modeling of the buck-boost converter

Bidirectional buck-boost converters are mainly used to regulate the output voltage to follow a given reference. They are a key device to interface storage elements and ensure continuous flow of power in renewable energy systems despite the fluctuations due to changes in weather conditions. The bidirectional buck converter (Fig. 2) consists of a switch network that generates the output signal by controlling the two switches Q_1 and Q_2. The input voltage v_{in} represents the voltage of the energy storage. v_0 is the voltage at the bidirectional converter terminal which needs to be regulated. L is the inductance of the converter and C_1, C_2 are the source and load side capacitors, respectively. It is assumed that the bidirectional converter is an ideal circuit. u is the control signal. When $u = 1$, Q_1 is on and Q_2 is off. When the control signal $u = 0$, Q_1 is off and Q_2 is on.

The state space averaged model of the bi-directional converter is given by [24]:

$$\begin{bmatrix} \frac{di_L}{dt} \\ \frac{dv_o}{dt} \end{bmatrix} = \begin{bmatrix} 0 & \frac{u}{L} \\ -\frac{u}{C} & \frac{1}{RC} \end{bmatrix} \begin{bmatrix} i_L(t) \\ v_o(t) \end{bmatrix} + \begin{bmatrix} -\frac{1}{L} \\ 0 \end{bmatrix} v_{in}(t) \tag{9}$$

where $i_L(t)$ is the inductor current, R is the equivalent resistance of the attached network, u is the control signal, and v_0 is the terminal voltage.

Taking the state variables as the tracking error of the output voltage, $x_1 = v_o - v_o^{ref}$ and its derivative x_2, yields the following state space model:

$$\begin{bmatrix} \dot{x}_1 \\ \dot{x}_2 \end{bmatrix} = \begin{bmatrix} 0 & 1 \\ \frac{u}{LC} & -\frac{1}{RC} \end{bmatrix} \begin{bmatrix} x_1 \\ x_2 \end{bmatrix} + \begin{bmatrix} 0 \\ uv_{in} + uv_o^{ref} \end{bmatrix} \frac{1}{LC} \tag{10}$$

where, v_o^{ref} represents the reference output voltage.

Our control objective is to effectively mitigate dynamic instability resulting from grid faults, mismatched uncertainties and parameter variations. Hence, we propose the FOSMC-based robust control approach detailed in the next section. This choice is motivated by the powerful robust properties of FOSMC as well as its flexible implementation to power converters.

3. FOSMC control design

Sliding mode control is a variable structure control method that is well known for its robustness to disturbances and parameter variations. Since power electronic converters inherently include switching devices, sliding mode control offers the ideal solution to implement a control which exploits the inherent variable structure nature of power electronic converters. However, the chattering phenomenon originated from the interaction between high-frequency switching and system's parasitic dynamics, limits its implementation in systems requiring high dynamic performance [25]. Additionally, finite time convergence cannot be guaranteed with standard SMC. Fractional order controllers, on the

other hand, have the potential to yield an open-loop transfer function in the form of fractional order integrator, thus providing a controlled system that is robust to changes in the process gain [34]. Additionally, the added extra degree of freedom in fractional order controllers results in better dynamic performance and more reliable control designs than its integral order counterpart [43].

Motivated be the above advantages, we derive in what follows an FOSM approach for the DFIG-based energy system.

3.1. Fundamentals of fractional-order control

Fractional-order controls are designed by substituting conventional integer-order integral/derivative actions by their fractional-order counterparts. Fractional order controllers are more robust and precise than classical controllers. They are developed with the aid of fractional-order calculus and yield stronger and more adaptive design to fulfill the system specifications [34]. In what follows, we briefly introduce some fundamental definitions and properties of fractional order calculus [34,43] that are used in deriving the FOSMC.

Definition. The Caputo definition of the αth order fractional-order derivative of a continuous function $f(t)$ is given by:

$$D^\alpha f(t) = \frac{1}{\Gamma(m-\alpha)} \int_0^t \frac{f^{(m)}(\tau)}{(t-\tau)^{\alpha-m+1}} d\tau \tag{11}$$

where $\Gamma(.)$ is the well-known Euler Gamma function. D^α denotes the derivative operator of order $\alpha \in \mathbb{R}^+$ and m is a positive integer, such that $m-1 < \alpha < m, m \in \mathbb{N}$.

The following are some of the main properties of fractional order derivative.

Property 1. (*[44]*) *If the Riemann-Liouville derivative $D_{t_0,t}^\beta f(t)$ ($m-1 < \beta < m$) of a function $f(t)$ is integrable, then:*

$$D_t^{-\alpha}\left(D_t^\beta f(t)\right) = D_t^{\beta-\alpha} f(t) - \sum_{j=1}^m \left[D_t^{\beta-j} f(t)\right]_{t=t_0} \frac{(t-t_0)^{\alpha-j}}{\Gamma(1+\alpha-j)} \tag{12}$$

Property 2. (*[43]*) *The fractional order calculus and the integer order calculus have the same linearity property.*

$$D^\alpha(af(t) + bg(t)) = aD^\alpha f(t) + bD^\alpha g(t) \tag{13}$$

Property 3. *When $\alpha = n$, $D^\alpha f(t)$ becomes integer order calculus, and when $\alpha = 0$ [43],*

$$D^0 f(t) = f(t) \tag{14}$$

Lemma 1. *Considering an integrable function $f(t)$ and at least one $t_1 \in \{0, t\}$, such that $f(t_1) \neq 0$, yields $I^\alpha |f(t)| \geq L$. with L being a constant [45].*

Lemma 2.. *If the fractional order system reaches an equilibrium point where $x = 0$ [46],*

$$D^\alpha x(t) = f(x,t) \tag{15}$$

Assuming Lipschitz condition is fulfilled by $f(x,t)$ where $\alpha \in \{0,1\}$.

Another assumption is made that the Lyapunov function, $V(t,x(t))$ and class-k functions $\alpha_i(i = 1, 2, 3)$ would satisfy the following conditions:

$$\alpha_1(\|x\|) < V(t,x(t)) < \alpha_2(\|x\|) \tag{16}$$

$$D^\alpha V(t,x(t)) < -\alpha_3(\|x\|) \tag{17}$$

Consider the following dynamic equations of a system with mismatched disturbances:

$$\begin{cases} D^\alpha x_1 = x_2 + d(t) \\ D^\alpha x_2 = a(x) + b(x)u \end{cases} \tag{18}$$

where x_1 and x_2 are the system's state variables, $u(t)$ is the control signal input. $d(t)$ is an unknown function representing the external disturbances, whereas $a(x)$ and $b(x)$ are derived from the state space model of the system under consideration.

The following assumptions are considered about the external disturbance $d(t)$.

Assumption 1. $d(t)$ is unknown but bounded, with $d^* = \sup|d(t)|$, $t > 0$

Assumption 2. $d(t)$ can be differentiated given that: $\lim\limits_{t\to\infty} \dot{d}(t) = 0$

System (18) can be represented in state space form as follows:

$$D^\alpha X = F(X) + G_1(X)u + G_2(x)d \tag{19}$$

where

$$X = [x_1, x_2]^T, F(X) = [x_2, a(x)]^T, G_1(x) = [0, b(x)]^T, G_2(X) = [1, 0]^T \tag{20}$$

The nonlinear disturbance observer considered to estimate the mismatched disturbances is given by:

$$\begin{aligned} \dot{p} &= -\ell G_2(X)p - \ell\big[G_2(X)\ell X + F(X) + G_1(X)u\big] \\ \widehat{d} &= p + \ell X \end{aligned} \tag{21}$$

where p represents the internal state of the disturbance observer, ℓ denotes the observer gain, $\widehat{d}$ is the disturbance estimation.

Lemma 3. *Selecting the observer gain, ℓ such that $e^2 e(t) = 0$ guarantees the global asymptotic stability of the observer* [47].

3.2. Fractional order sliding mode control design

There are two steps to design the sliding mode controller. The first step is to design a sliding manifold, so that the sliding motion satisfies the design specifications. The second step entails the design of a control law to enforce the sliding mode [24].

In order to achieve a constant output voltage at PCC despite input voltage disturbances and load variations, we define the following nonlinear sliding surface:

$$\sigma = \varphi_1 x_1 + \varphi_2\big(x_2 + \widehat{d}\big) \tag{22}$$

where $\widehat{d}$ is the estimate of the disturbance d. φ_1 and φ_2 are positive integers that should be chosen to ensure a balance between the asymptotic stability and the magnitude of chattering.

Computing the time derivative of (22), yields:

$$\dot{\sigma} = \varphi_1 \dot{x}_1 + \varphi_2\Big(\dot{x}_2 + \dot{\widehat{d}}\Big) \tag{23}$$

Hence, $\dot{x}_2 = \frac{1}{\varphi_2}(-\varphi_1 \dot{x}_1 - \varphi_2 \dot{\widehat{d}})$ and:

$$D^\alpha x_2 = -\frac{\varphi_1}{\varphi_2} D^\alpha x_1 - D^\alpha \widehat{d} \tag{24}$$

Using (18) and (24), we get,

$$D^\alpha x_2 = a(x) + b(x)u = -\frac{\varphi_1}{\varphi_2} D^\alpha x_1 - D^\alpha \widehat{d} \tag{25}$$

From (25) we can synthesize the equivalent control law defined by:

$$u_{eq} = \frac{1}{b(x)}\Big(-\frac{\varphi_1}{\varphi_2} D^\alpha x_1 - a(x) - D^\alpha \widehat{d}\Big) \tag{26}$$

Expressing (10) in fractional order derivative, yields:

$$\begin{aligned} D^\alpha x_2 &= \frac{u}{LC} x_1 - \frac{1}{RC} x_2 + \frac{v_{in} + v_o^{ref}}{LC} u \\ &= -\frac{1}{RC} x_2 + \frac{v_{in} + v_o^{ref} + x_1}{LC} u \end{aligned} \tag{27}$$

Comparing (27) with (10), yields:

$$a(x) = \frac{-x_2}{RC}, b(x) = \frac{v_{in} + v_0^{ref} + x_1}{LC} \tag{28}$$

Substituting (26) into (23) yields:

$$\dot{\sigma} = \varphi_1 \dot{x}_1 + \frac{\varphi_2 u}{LC}\big(x_1 + v_{in} + v_{ref}\big) - \frac{\varphi_2 x_2}{RC} + \varphi_2 D^\alpha \widehat{d} = 0 \tag{29}$$

The equivalent control can be expressed as:

$$u_{eq} = \frac{1}{\frac{x_1 + v_{in} + v_o^{ref}}{LC}}\left[-\frac{\varphi_1}{\varphi_2} D^\alpha x_1 - \Big(-\frac{x_2}{RC}\Big) - D^\alpha \widehat{d}\right] \tag{30}$$

The equivalent control function in (30) facilitates the discontinuous control for the nonlinear sliding manifold in (22). The reaching law u_r is introduced to ensure the sliding mode is attained in finite time.

$$u_r(t) = -D^{\alpha-1}\big(\varepsilon_1 \sigma(t) + \varepsilon_2 sign(\sigma(t))|\sigma(t)|^\delta\big) \tag{31}$$

$$D^\alpha \widehat{d} = \varphi_c D^{\alpha-1} sign(\sigma(t)) \tag{32}$$

where $\varepsilon_1, \varepsilon_2$ are constant gains, and $\delta \in (0,1)$. ε_1 is a proportional rate term which influences the convergence rate of the states to the sliding manifold (the larger σ, the faster the convergence rate). ε_2 and δ make the reaching law increase the reaching speed when the state is far away from the switching manifold but reduces the rate when the sliding mode is reached.

Combining the equivalent control law (30) with the reaching law (31), yields:

$$\begin{aligned} u(t) = \frac{1}{b(x)}\Big(-\frac{\varphi_1}{\varphi_2} D^\alpha x_1 - a(x) - \varphi_c D^{\alpha-1} sign(\sigma)\Big) - D^{\alpha-1}(\varepsilon_1 s \\ + \varepsilon_2 sign(\sigma)|\sigma|^\delta) \end{aligned} \tag{33}$$

Theorem. *The control law in (33) and the fractional order dynamic system with mismatched disturbances in (18) are stable and will converge in finite time.*

Proof:. Defining the following Lyapunov function:

$$V = \frac{1}{2}\sigma^2 \tag{34}$$

And assuming $D^k \sigma$ are bounded such that:

$$\|D^k \sigma\| \leqslant M \tag{35}$$

Along the real axis, the Gamma function is a non-zero element and Gamma function of any complex number is non-zero, therefore, the reciprocal of any Gamma function is an entire function. For a lower bound of L, $0 < L \leq |\Gamma(1-\alpha+k)|$ where, $k = 1,2,3,...$

Convergence of $\Gamma k/\Gamma(k+1) = 1/k$ and $\sum_{k=1}^{\infty} 1/\Gamma(k+1)$ entails the existence of an upper bound H such that:

$$0 < \sum_{k=1}^{\infty} 1/\Gamma(k+1) < H \tag{36}$$

In light of the above discussions, the following assumption can be made [48]:

$$\left|\sum_{K=1}^{\infty} \frac{\Gamma(1+\alpha)}{\Gamma(1+k)\Gamma(1-k+\alpha)} D^k \sigma D^{\alpha-k} \sigma\right| \leqslant \beta|\sigma| \tag{37}$$
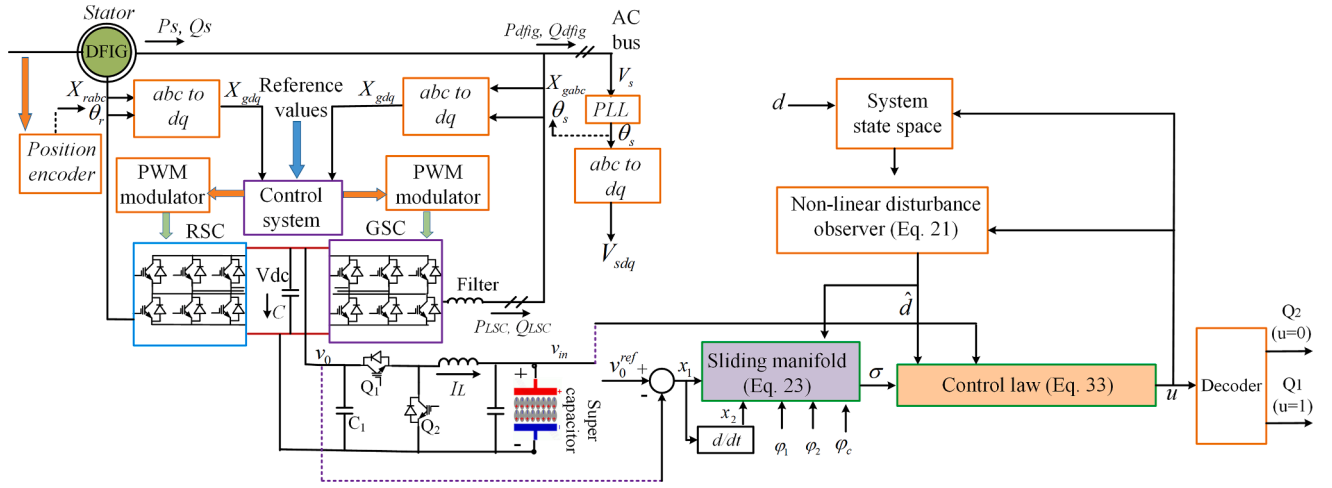
Fig. 3. Proposed control topology.

where β is a constant and it is positive.

Using assumption (37), and evaluating the fractional order derivative of (22) yields,

$$D^{\alpha}V \leqslant \sigma D^{\alpha}\sigma + \left| \sum_{K=1}^{\infty} \frac{\Gamma(1+\alpha)}{\Gamma(1+k)\Gamma(1-k+\alpha)} D^{k}\sigma D^{\alpha-k}\sigma \right| \leqslant \sigma D^{\alpha}\sigma + \beta|\sigma| \quad (38)$$

Differentiating the sliding surface,

$$D^{\alpha}\sigma = \varphi_1 D^{\alpha}x_1 + \varphi_2 D^{\alpha}x_2 + \varphi_2 D^{\alpha}\widehat{d} \quad (39)$$

Substituting (18), (32), and (39) to (38) yields:

$$D^{\alpha}V \leqslant \sigma \left(\varphi_1 D^{\alpha}x_1 + \varphi_2 D^{\alpha}x_2 + \varphi_2 \varphi_c D^{\alpha-1} sign(\sigma(t)) \right) + \beta|\sigma|$$
$$D^{\alpha}V \leqslant \sigma \left\{ \varphi_1 D^{\alpha}x_1 + \varphi_2(a(x) + b(x)u) + \varphi_2 \varphi_c D^{\alpha-1} sign(\sigma(t)) \right\} + \beta|\sigma| \quad (40)$$

Substituting u from (33) into (40) and using sign $(\sigma)\sigma=|s|$ and $sign^2(\sigma) = 1$ yields:

$$D^{\alpha}V \leqslant -\varphi_2\varphi_c|\sigma| - \varphi_2\varepsilon_1 b(x)|\sigma| - \varphi_2\varepsilon_2 b(x)|\sigma| + \beta|\sigma| + \varphi_2\varphi_c|\sigma| \quad (41)$$

$$D^{\alpha}V \leqslant |\sigma|\left(-\varphi_2\varphi_c - \varphi_2\varepsilon_1 - \varphi_2\varepsilon_2 + \beta + \varphi_2\varphi_c \right) \leqslant |\sigma|\left(-\varphi_2(\varepsilon_1 + \varepsilon_2) + \beta \right) \quad (42)$$

Considering property 1 and integrating (39) between 0 and t_r, yields:

$$V(t_r) - V^{\alpha-1}(0)\frac{(t_r)^{\alpha-1}}{\Gamma(\alpha)} \leqslant (-\varphi_2(\varepsilon_1 + \varepsilon_2) + \beta)D^{-\alpha}|\sigma| \quad (43)$$

Applying Lemma 1 and considering $s(t_r) = 0$, yields:

$$-V^{\alpha-1}(0)\frac{(t_r)^{\alpha-1}}{\Gamma(\alpha)} \leqslant (-\varphi_2(\varepsilon_1 + \varepsilon_2) + \beta)L \quad (44)$$

$$\frac{(t_r)^{\alpha-1}}{V^{\alpha-1}(0)} \leqslant \Gamma(\alpha)L(\varphi_2(\varepsilon_1 + \varepsilon_2) - \beta) \quad (45)$$

$$t_r \leqslant \left(\frac{\Gamma(\alpha)L(k_2(\varepsilon_1 + \varepsilon_2) - \beta)}{V^{\alpha-1}(0)} \right)^{1-\alpha} \quad (46)$$

Thus, the error dynamics will converge to zero in finite time.

3.3. Super-capacitor energy storage system

To further improve the fault ride through capability of the system and deliver a stabilized power to the grid, we install a super-capacitor as energy storage system. This choice is motivated by their high charging/discharging rates and low maintenance requirements along with the continuous decrease in their cost per unit energy as a result of recent advances in power electronics. An added advantage of using a super-
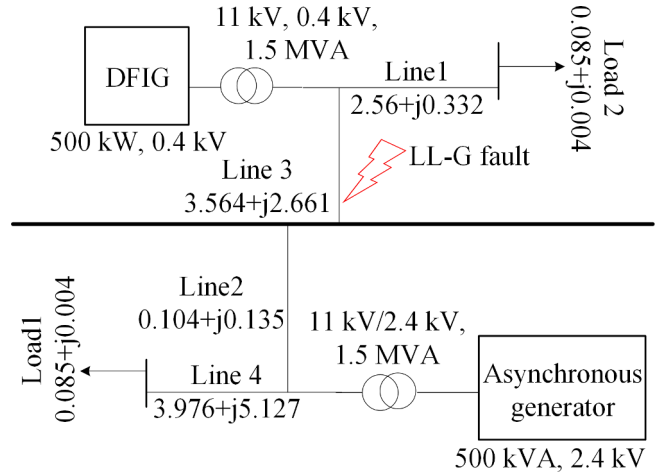

Fig. 4. Small scale power supply test network considered for the validation of the proposed strategy.

capacitor in our scheme is preventing the triggering of the built-in crowbar system, for operating conditions other that emergency situations during which the proposed scheme fails to provide the required protection. That is, to stop the crowbar from being triggered by faulty conditions, the dc-link voltage surges occurring during fault starts and clearance need to be limited to a predefined limit by ensuring that the response time of the proposed controller is fast enough. Utilizing the super-capacitor as supplemental energy source will guarantee the fast response.

The proposed control scheme is outlined in Fig. 3. The dc-link voltage at the power conditioning circuit terminal is the voltage that would be regulated by the dc/dc converter. The terminal voltage will be regulated to the fixed rated dc-link voltage. When the control signal u = 1, the switch Q_1 will be on and Q_2 will be off. The converter will then work as a buck converter. In this case, the super-capacitor will be charging. On the other hand, if the control signal u = 0, then Q_2 will be on and Q_1 will be off. The converter will work as a boost converter. The switching of Q_1 and Q_2 is mutually exclusive. The switching of the converter is determined by the FOSMC controller. The aim of the bidirectional converter is to regulate the output voltage, v_0 to a reference value, v_0^{ref}. The same technique can also be helpful for regulating DFIG power output during any network events. In this paper, this strategy is implemented to mitigate the dynamic instability in the DFIG system caused by grid faults.
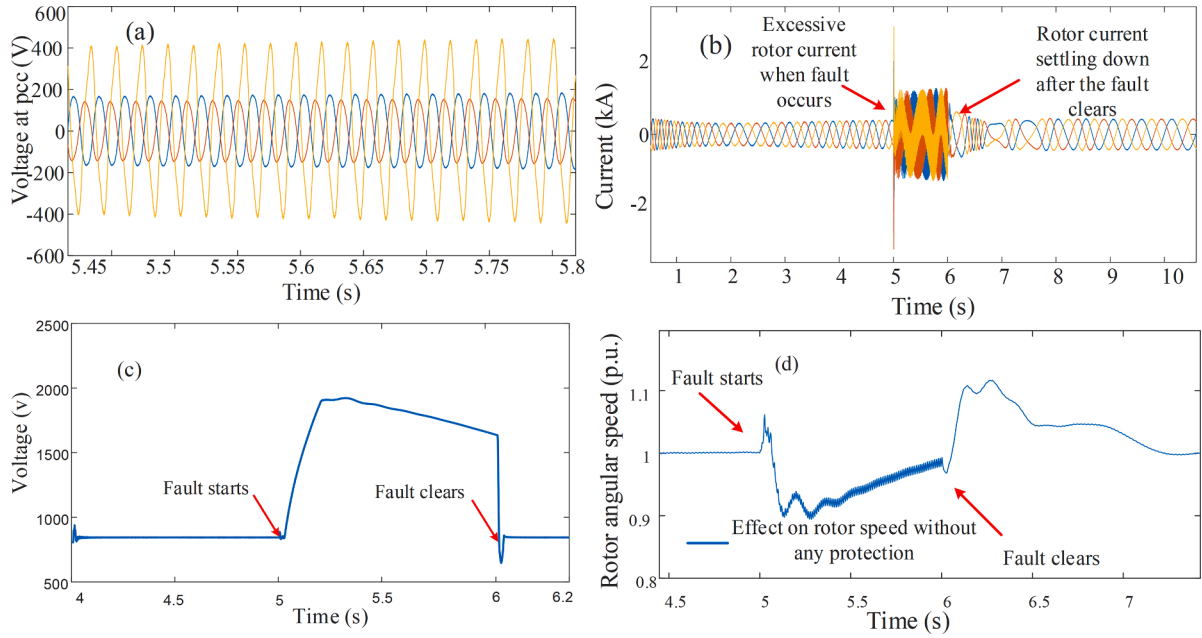
Fig. 5. Performance without implementing the proposed topology: (a) PCC voltage at feeder 1; (b) DFIG rotor current; (c) DFIG dc-link voltage; (d) rotor angular speed.

4. Computer experiments

The proposed control topology is implemented to the small-scale power supply test network [49] depicted in Fig. 4. This network consists of a conventional asynchronous generator and a DFIG-based wind energy system. The system parameters are illustrated in Appendix B.

In order to assess the ability of the control topology to properly mitigate the effects of faults and improve the transient stability of the wind energy system, we consider a double line to ground (LL-G) fault near the bus to which the DFIG is connected (Fig. 4).

To better assess the dynamic performance of the proposed topology, we first analyze the system's performance with the above conditions, but without implementing the proposed topology. The obtained results under those circumstances are shown in Fig. 5(a)-(c).

Note that, upon fault occurrence (at 5 sec), the voltage at PCC sags deeply as shown in Fig. 5(a). The rotor current exhibits high increases resulting from the short circuit current surge in the stator coil (Fig. 5(b)). Note that the surge in current results in an increase of $>2V_{dc}$ in the dc-link voltage (Fig. 5(c)) during grid faults.

Note that the electromagnetic torque is also affected by the grid fault. This latter yields a sudden change in the power demand. Also, when the fault clears, the load demand is restored. The active power mismatch triggered by the grid fault results in significant fluctuations in the rotor angular speed as shown in Fig. 5(d), thereby causing high torsional stress on the drivetrain. Therefore, during fault, the DFIG experiences significant fluctuations in the rotor angular speed or electromagnetic torque. Rapid torque fluctuations significantly stress the drive shaft of the wind turbine and reduce its reliability.

4.1. Performance of the proposed FOSMC scheme

In this section, we assess the system performance with the proposed FOSMC-based approach and under the same LL-G fault. Additionally, to further validate the robustness of the proposed approach against mismatched disturbances, we introduce an additional 15% increase in the nominal values of the rotor andtator resistances. The system responses under those circumstances are shown in Fig. 6. The FOSMC parameters are provided in Table 3 of Appendix B. Note the significant improvement in the dc-link voltage dynamics and the controller's ability to regulate it

to near its reference value (Fig. 6(a)). The dc-link voltage fluctuations, V_{dc} are limited by 5 V. The supplemental energy supplied by the super-capacitor further facilitates the mitigation of the voltage surge during fault occurrence. Note that as a result of the better regulated dc-link voltage, the GSC is not overloaded. Fig. 6(b) shows the dynamics of the GSC d-current. The GSC d-current is 0.2 pu which suggest a normal loading condition. It is worth stressing that high loading causes thermal stress in the converter's semiconductor junction [52]. Since, the GSC-loading is normal, the junction temperature is steady as shown in Fig. 6(c). The maximum junction temperature is below 120° and magnitude of the temperature cycles are also steady C during grid faults. Fig. 6(d) shows that the proposed control approach significantly reduces the fluctuations in the rotor angular speed during fault occurrence by limiting the fluctuations to ± 0.003 pu. The dynamics of the super-capacitor current is presented in Fig. 6(e). It shows that a large amount of current is absorbed by the super-capacitor thereby preventing dangerous current surges and further improving the transient stability of the wind energy system. Even after the fault clears, mitigation of the voltage fluctuations is facilitated by the super-capacitor support. The state-of-charge (SoC) of the battery is shown in Fig. 6(f). Note that the SoC keeps rising during the fault period as it keeps absorbing the current from the dc-link. The SoC rises to 74.486% from 74.482% very fast and then starts to reduce again after fault clears. Fig. 6(g) shows the rotor current with high fluctuations when the fault starts and clears. The fluctuations are more than twice the rating since the dc/dc converter cannot directly mitigate the surge in rotor flux. Fig. 6(h) shows the controller output signal which is the switching command for the dc/dc converter. Fig. 6(i) shows the disturbance estimation error by the disturbance observer.

4.2. Comparison with SSMC

To further assess the performance of the proposed topology, we exchanged the FOSMC approach by the SSMC approach proposed in [50]. Non-linear disturbance observer and sliding manifold are used. The sliding surface for the SSMC, $\sigma = V_0^{ref} - V_0$. The control objective is to switch between two constant values 1 or 0 when the error dynamic reaches the hyperplane $\sigma = 0$. When the error, $\sigma > 0$, control law makes the $\dot{\sigma} < 0$ and when $\sigma < 0$, control law makes the $\dot{\sigma} > 0$, thus the case
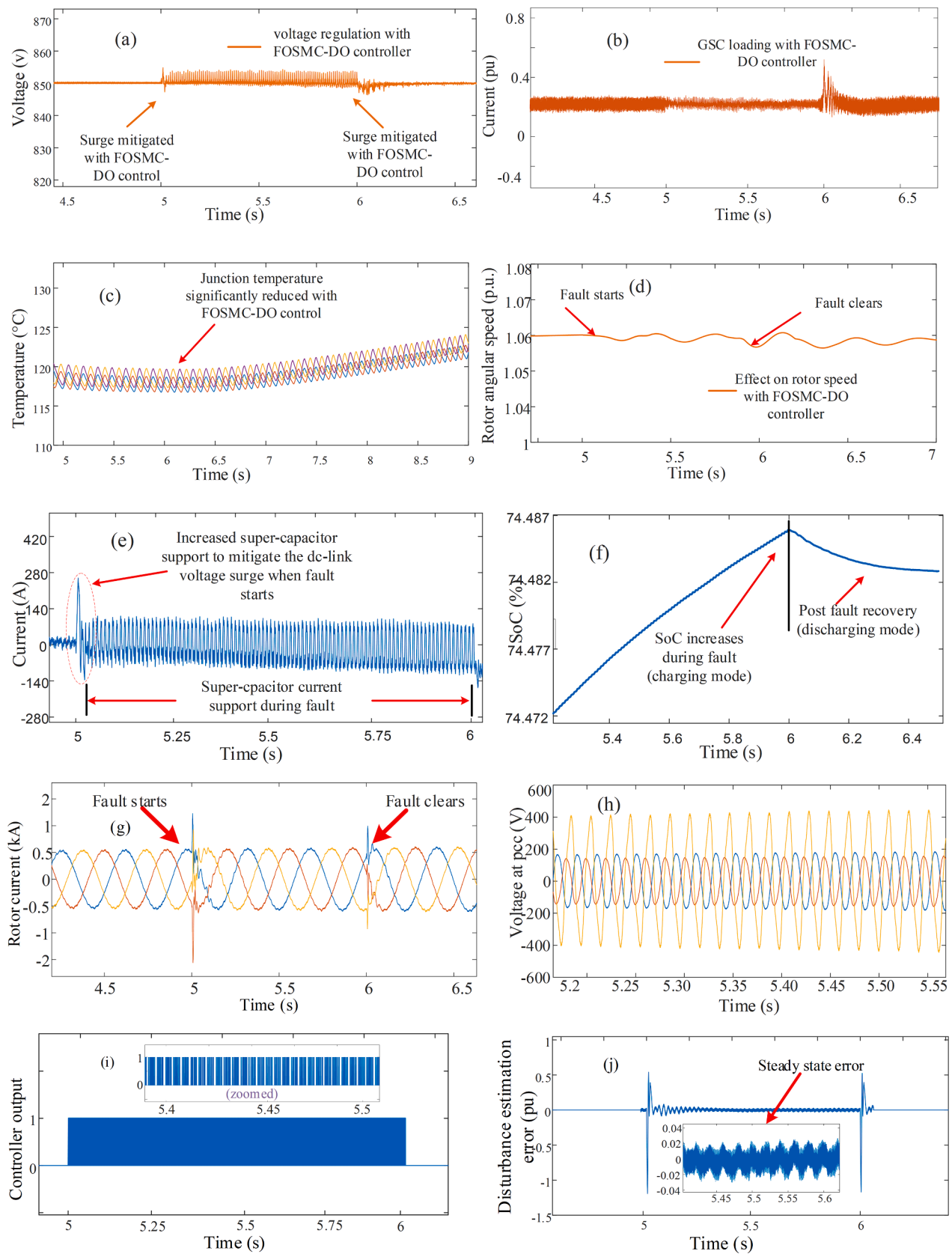
Fig. 6. Dynamics with the proposed topology: (a) dc-link voltage; (b) GSC d-current; (c) GSC junction temperature; (d) rotor angular speed; (e) super-capacitor current; (f) super-capacitor state of charge; (g) rotor current; (h) PCC voltage; (i) controller output signal; (j) disturbance estimation error.
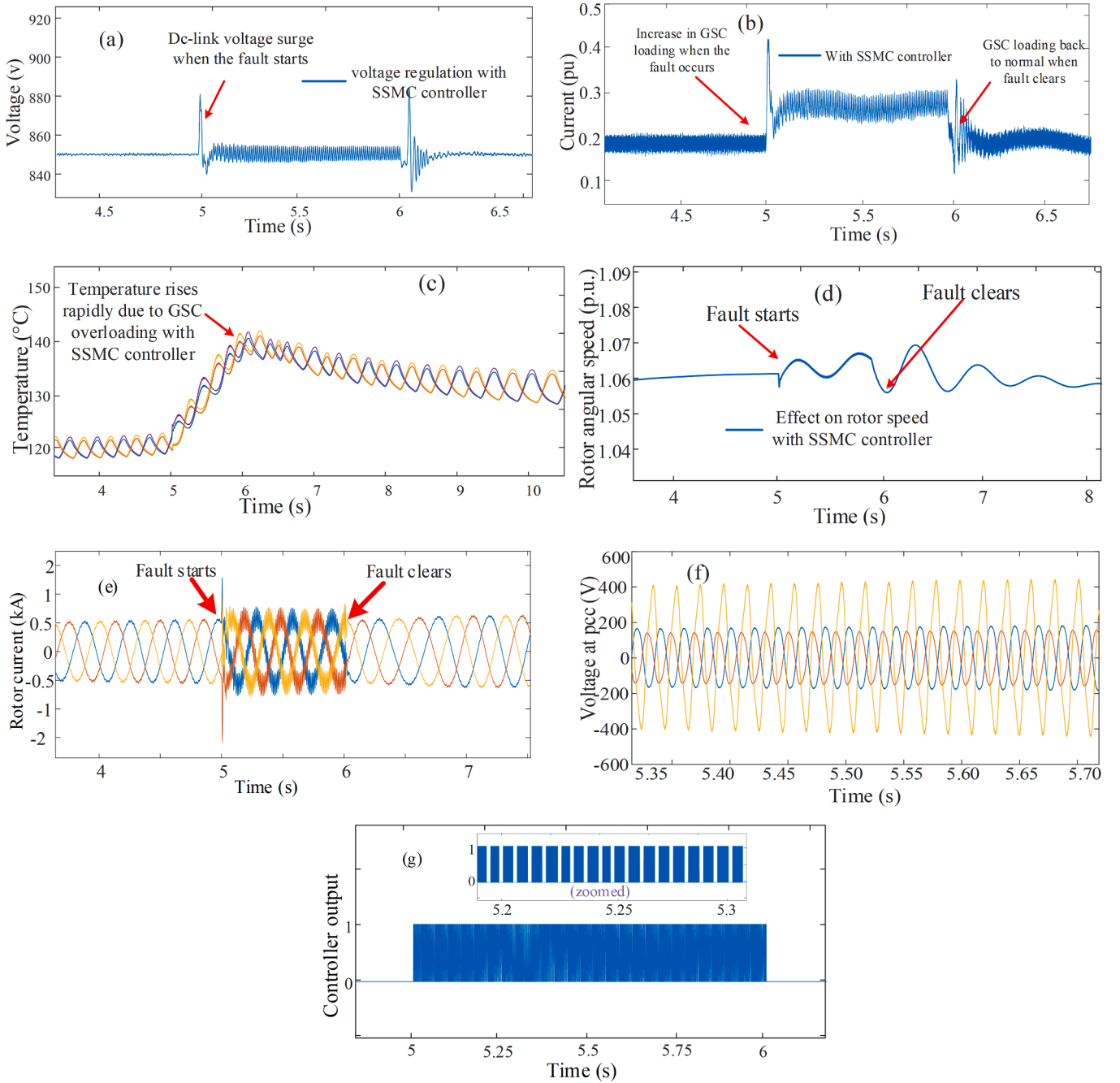
Fig. 7. Dynamics under faulty conditions and with the SSMC controller: (a) dc-link voltage; (b) GSC d-current; (c) semiconductor junction temperature; (d) rotor angular speed; (e) rotor current; (f) PCC voltage; (g) controller output signal.

$\sigma\dot{\sigma}<0$ always holds, until the hyperplane $\sigma = 0$ is reached. The nonlinear disturbance observer provides the estimation of the mismatched disturbance which is used to compensate the sliding manifold. However, instead of fractional order, integer order system is considered. The derived control laws denote the reference signals for the PWM modulator. Nevertheless, the DFIG-based wind energy system configuration remains totally unchanged. Only the converter controller is replaced. The dynamics of the DFIG-based wind energy system in this case is illustrated in Fig. 7. Note, the higher surge in dc-link voltage during the grid fault (Fig. 7(a)) compared to the FOSMC (Fig. 6(a)). The dc-link voltage fluctuations, ΔV_{dc} are as high as 30 V. This high dc-link voltage poses a risk of triggering the crowbar which would exacerbate the voltage condition at PCC. It is worth noting, however, that the dc-link voltage fluctuations observed with the SSMC are still being

regulated below the limit, nonetheless, its magnitude is still higher than that of the proposed FOSMC. This has the potential to trigger an increase in the GSC current to mitigate for the fluctuations in the dc-link voltage. The GSC d-current increases to 0.27 pu to mitigate the dc-link fluctuations. Note also the noticeable chattering phenomena in the voltage and current dynamics. The junction temperature of the GSC is shown in Fig. 7(c). The maximum junction junction temperature increaes to 140 °C quite fast. Note the increase in the temperature fault occurrence as a results of the GSC overloading. Upon fault clearance, the junction temperature starts to go back to its initial value. Fig. 7(d) depicts the dynamics of the rotor angular speed. The fluctuation increases as high as 0.1 pu. Note that even after the fault clearance at 6 s, the transients in the rotor speed take a while to be mitigated. Fig. 7(e) shows the rotor current. Rotor current increases to a high value when the fault and starts

and clears. Also, note the unstable current during grid fault. Fig. 7(f) shows the controller output signal which the switching signal for dc/dc converter.

As seen from the above results, the FOSMC-based control scheme provides superior performance than the SSMC-based control scheme, even with the disturbances introduced in the system. The dynamic instability in the DFIG caused by the grid fault is effectively mitigated by the clever combination of the robustness properties FOSMC approach with the high capacitance and power density of the super-capacitor.

4.3. Comparison in terms of computational complexity

In this section, the FOSMC and SSMC are compared in terms of computational requirements. The computer simulations are carried out in MATLAB/Simulink environment. The processor of the computer is an Intel Core i7 Octa Core processor with 3.6 GHz clock speed and 16 MB cache memory. Similar to [51], the computational complexity is measured in terms of program runtime, CPU load, and steady state error. Once the program is executed, the runtime is updated. This process is carried out for 200,000 samples, and the corresponding values are averaged accordingly. The obtained computational parameters for both approaches are illustrated in Table 4. Note that both approaches exhibit identical run times, however the CPU load is higher for the FOSMC.

5. Conclusion

This paper proposed a control topology that enhances the transient stability of wind energy systems by integrating the robust performance of FOSMC with the high charging/discharging rate of super-capacitors. The contributions of this article can be summarized as follows.

- An FOSMC-based approach that effectively regulates the dc link voltage to near its rated value and mitigates dynamic instability resulting from grid faults and disturbances.

- A design that implements a super-capacitor as additional energy storage element to prevent dangerous voltage surges and stabilize power mismatches resulting from grid faults.
- A design that prevents converter overloading (the grid side converter loading was regulated at 0.2 pu (below its rated value)).
- A design that successfully bypasses the crowbar system and circumvents its drawbacks.
- A design that is robust against both, matched and mismatched disturbances.
- A comparison with a SSMC approach showed an improvement in the maximum fluctuations of the dc-link voltage by 83% and a 20 °C reduction in maximum junction temperature under faulty conditions.

Our future work will focus on further assessing the performance of the proposed approach using industrial experimental settings, implementing the proposed approach to hybrid renewable energy sources and extending the performance analysis to encompass a wider range of grid faults and disturbances encountered in distribution networks with renewable energy sources.

CRediT authorship contribution statement

Md Nafiz Musarrat: Conceptualization, Methodology, Validation, Writing - original draft. **Afef Fekih:** Conceptualization, Methodology, Validation, Writing - review & editing, Supervision.

Declaration of Competing Interest

The authors declare that they have no known competing financial interests or personal relationships that could have appeared to influence the work reported in this paper.

Appendix A. Semiconductor loss and junction temperature calculation

The GSC typically becomes overloaded as it tries to regulate the fluctuations of the dc-link voltage. GSC overloading results in increased thermal loss, thereby increasing the temperature of the converter's semiconductor junctions. The high thermal stress drastically reduces the converter's reliability. Semiconductor losses are of two types: switching loss and conduction loss. The overloading of the GSC causes conduction losses in the semiconductors. The conduction energy loss of the IGBT and freewheeling diode can be expressed as [52]:

$$EcondIGBT(i_T, Tj) = \int_0^T i_T(t)\big(V_{ce0}(T_j) + r_{ce}(T_j)i_T(t)\big)dt \tag{i}$$

$$EcondDiode(i_T, Tj) = \int_0^T i_D(t)\big(V_{fe0}(T_j) + r_f(T_j)i_D(t)\big)dt \tag{ii}$$

where $E_{condIGBT}$ and $E_{conDiode}$ are the conduction loss of IGBT and diode, T_j is the junction temperature, i_T and i_D are the currents through IGBT and diode, V_{ce0} and V_{f0} denote forward voltage of IGBT and diode, and r_f and r_{ce} denote bulk resistance of diode and IGBT.

A detailed discussion about semiconductor loss and its effect on junction temperature can be found in [51]. A brief explanation of loss calculations is provided here. A two-cell Cauer thermal network is used to calculate the semiconductor junction temperature. The thermal resistances and capacitances of the thermal network determines the thermal loss efficiency of the semiconductors. If the thermal output is high, the temperature of the converter case will be lower which is dependent on the efficiency of the heat sink and ambient temperature. The junction temperatures of IGBT and diodes are determined by Cauer network, which considers the case temperature and semiconductor power losses as inputs. The semiconductor power losses are calculated by two separate blocks for IGBT and diodes. These blocks calculate the losses based on the mathematical formula for switching and conduction losses. The formulas for conduction loss are given in (i) and (ii).

Appendix B

See Tables 1–3.

Table 1

DFIG parameter values.

Parameter	Value
Turbine inertia constant	4.32 s
Stator terminal voltage	400 V
DC link voltage	850 V
X_m	2.3 Ω
R_s	0.023 Ω
X_s	0.18 Ω
R_r	0.016 Ω
X_r	0.16 Ω

Table 2

Buck-boost converter parameters.

Parameter	Value
Rated voltage of the supercapacitor	500 V
Capacitance of the supercapacitor	500 F
L	4.5 mH
C_1	1200 μF
C_2	1200

Table 3

FOSMC parameters.

Parameter	Value
α	0.9
δ	0.99
φ_1, φ_2	67,10
φ_c	0.3
L	70
$\varepsilon_1, \varepsilon_2$	25, 25

Table 4

Computational parameters.

Controller	Parameter	Values
FOSMC	Program runtime	1.37 μs
	CPU load	4.02%
	Steady state error	Medium
SSMC	Program runtime	1.37 μs
	CPU load	7.4%
	Steady state error	Negligible

Note, also, that the steady state error performance is much better when using the FOSMC.

References

[1] IRENA. Future of Wind: deployment, investment, technology, grid integration and socio-economic aspects (A Global Energy Transformation paper. International Renewable Energy Agency, Abu Dhabi, 2019.

[2] Jerin A, Kaliannan P, Subramanian U. Improved fault ride through capability of DFIG based wind turbines using synchronous reference frame control based dynamic voltage restorer. ISA Trans 2017;70:465–74.

[3] Morshed MJ, Sardoueinasab Z, Fekih A. "A coordinated control for voltage and transient stability of multi-machine power grids relying on wind energy. Int J Electrical Power Energy Syst July 2019;109:95–109.

[4] Artigao E, Martín-Martínez S, Honrubia-Escribano A, Gómez-Lázaro E. Wind turbine reliability: A comprehensive review towards effective condition monitoring development. Appl Energy 2018;228(113309):1569–83.

[5] Shafiee MR, Shahbabaei Kartijkolaie H, Firouzi M, Mobayen S, Fekih A. A dynamic multi-cell FCL to improve the fault ride through capability of DFIG-based wind farms. Energies November 2020;13:6071.

[6] Gebru F, Khan B, Alhelko H. Analyzing low voltage ride through capability of doubly fed induction generator based wind turbine. Comput Electr Eng 2020;86 (106727):1–19.

[7] Erlich I, Wrede H, Feltes C. Dynamic behavior of DFIG-based wind turbines during grid faults. Proc Power Convers Conf 2007;1195–200.

[8] Tohidi S, Mohammadi-ivatloo B. A comprehensive review of low voltage ride through of doubly fed induction wind generators. Renew Sustain Energy Rev May 2016;57:412–9.

[9] Jerin AR, Kaliannan P, Subramaniam U, El Moursi MS. Review on FRT solutions for improving transient stability in DFIG-WTs. IET Renewable Power Generat Aug. 2018;12(15):1786–99.

[10] Zhang L, Jin X, Zhan L. A novel LVRT control strategy of DFIG based rotor active crowbar. In: Proc. of Asia-Pacific power and energy engineering conference, Wuhan, China, 2011. p. 25–28.

[11] Jalilian A, Naderi SB, Negnevitsky M, Hagh M, Tarafdar M, Muttaqi K. Controllable DC-link fault current limiter augmentation with DC chopper to improve fault ride-through of DFIG. IET Renew Power Gen 2017;11(2):313–24.

[12] Yang G, Fletcher J, O'Reilly J. A series-dynamic-resistor-based converter protection scheme for doubly-fed induction generator during various fault conditions. IEEE Trans Energy Convers 2010;25:422–32.

[13] Tripathi P, Sahoo S, Chatterjee K. Enhancing the fault ride through capability of DFIG-based wind energy system using saturated core fault current limiter. J Eng 2019;2019(18):4916–21.

[14] Aktarujjaman M, Kashem M, Ledwich G. Smoothing output power of a doubly fed wind turbine with an energy storage system. In: IEEE Int. Conf. on Power Elec., Drives Energy Sys.; 2006. p. 2–6.

[15] Abbey C, Joos G. Energy storage and management in wind turbine generator systems. In: In Proc. IEEE Int. Power Elect. Motion Control Conf.; 2006. p. 2055–6.

[16] Mellincovsky M, Yuhimenko V, Peretz M, Kuperman A. Analysis and control of direct voltage regulated active DC-link capacitance reduction circuit. IEEE Trans Power Elec 2018;33(7):6318–32.

[17] Raju S, Pillai G. Design and implementation of type-2 fuzzy logic controller for DFIG-based wind energy systems in distribution networks. IEEE Trans Sustain Energy 2016;7(1):345–53.

[18] Zhang Z, Li Z, Kazmierkowski MP, Rodriguez J, Kennel R. Robust predictive control of three-level NPC back-to-back power converters PMSG wind turbine systems with revised prediction. IEEE Trans Power Electron 2018;33(11):9588–98.

[19] Li P, Wang J, Xiong L, Huang S, Ma M, Wang Z. Energy-shaping controller for DFIG-based wind farm to mitigate sub-synchronous control interaction. IEEE Trans. Power Syst 2020.

[20] Li P, Xiong L, Wu F, Ma M, Wang J. Sliding mode controller based on feedback linearization for damping of sub-synchronous control interaction in DFIG-based wind power plants. Int J Electr Power Energy Syst 2019;107:239–50.

[21] Yang B, Yu T, Shu H, Zhang Y, Chen J, Sang Y. Passivity-based sliding mode control design for optimal power extraction of a PMSG based variable speed wind turbine. Renewable Energy 2018;119:577–89.

[22] Yang B, Yu T, Shu H, Dong J, Jiang L. Robust sliding-mode control of wind energy conversion systems for optimal power extraction via nonlinear perturbation observers. Appl Energy 2018;210:711–23.

[23] Utkin V, Poznyak A, Orlov Y, Polyakov A. Road map for sliding mode control design. Springer Nature; 2020.

[24] Mehta A, Naik B. Sliding Mode Controllers for Power Electronic Converters. Springer Nature; 2019.

[25] Guldner J, Utkin V. The chattering problem in sliding mode systems. Proc. of Int. Symposium on Mathematical Theory of Networks and Systems. 2000.

[26] Morshed MJ, Fekih A. Integral terminal sliding mode control to provide fault ride-through capability to a grid connected wind turbine driven DFIG. In: Proc. of IEEE Int. Conf. Ind. Tech.; 2015. p. 1059–64.

[27] Liu J, Wang X. Fuzzy sliding mode control. In: Advanced Sliding Mode Control for Mechanical Systems. Berlin: Spring; 2011. p. 233–79.

[28] Utkin V, Poznyak A. Adaptive sliding mode control with application to super-twist algorithm: equivalent control method. Automatica 2013;49(1):39–47.

[29] Taleb M, Plestan F, Bououlid B. Higher order sliding mode control based on adaptive first order sliding mode controller. Proc IFAC. Vol 2014;47(3):1380–5.

[30] Benbouzid M, Beltran B, Amirat Y, Yao G, Han J, Mangel H. Second-order sliding mode control for DFIG-based wind turbines fault ride-through capability enhancement. ISA Trans 2014;53(3):827–33.

[31] Mei K, Ding S. Second-order sliding mode controller design subject to an upper-triangular structure. IEEE Trans Syst, Man, Cybernet: Syst 2018;15:1–11.

[32] Yang J, Li S, Yu X. Sliding-mode control for systems with mismatched uncertainties via a disturbance observer. IEEE Trans Indus Electr 2012;60(1):160–9.

[33] Pashaei S, Badamchizadeh M. A new fractional-order sliding mode controller via a nonlinear disturbance observer for a class of dynamical systems with mismatched disturbances. ISA Trans 2016;63:39–48.

[34] Monje C, Chen Y, Vinagre B, Xue D, Feliu V. Fractional-Order Systems and Controls. Fundamentals and Applications. Springer-Verlag; 2010.

[35] Gonzalez E, Tepljakov A, Concepción M, Petrás I. Retrofitting fractional-order dynamics to an existing feedback control system: from classical proportional-integral (PI) control to fractional-order proportional-derivative (FOPD) control. Int Res J Innovat Eng. Sci Technol 2017:1–6.

[36] Monje CA, Chen Y, Vinagre BM, Xue D, Feliu-Batlle V. Fractional Order Control strategies for power electronic buck converters. In: Fractional-order Systems and Controls. Springer; 2010. p. 365–90.

[37] Babes B, Boutaghane A, Hamouda N, Mezache M. Design of a Robust Voltage Controller for a DC-DC Buck Converter Using Fractional-Order Terminal Sliding Mode Control Strategy. Proc. of Int. Conf. on Advanced Eletrical Engineering. 2019.

[38] Xiong L, Wang J, Mi X, Khan MW. Fractional order sliding mode based direct power control of grid-connected DFIG. IEEE Trans Power Syst 2018;33(3):3087–96.

[39] Ebrahimkhani S. Robust fractional order sliding mode control of doubly-fed induction generator (DFIG)-based wind turbines. ISA Trans 2016;63:343–54.

[40] Yang B, Wang J, Sang Y, Yu L, Shu H, Li S, et al. Applications of super-capacitor energy storage systems in microgrid with distributed generators via passive fractional-order sliding-mode control. Energy 2019;187.

[41] Yang B, Wang J, Zhang X, Yu L, Shu H, Yu T, et al. Control of SMES systems in distribution networks with renewable energy integration: A perturbation estimation approach. Energy 2020;202.

[42] Monje CA, Chen Y, Vinagre BM, Xue D, Feliu-Batlle V. Fractional Order Systems and Controls. Springer; 2010.

[43] Podlubny I. Fractional-order systems and $PI^\lambda D^\mu$ controllers. IEEE Trans Automatic Control 1999;44:208–14.

[44] Tepljakov A, Petlenkov E, Belikov J. Robust FOPI and FOPID controller design for FFOPDT plants in embedded control applications using frequency-domain analysis. In: Proc. of the American control conf.; 2015. p. 3868–73.

[45] Aghababa MP. Design of a chatter-free terminal sliding mode controller for nonlinear fractional-order dynamical systems. Int J Control 2013;86:1744–56.

[46] Yan L, Chen Y, Podlubny I. Mittag–Leffler stability of fractional-order nonlinear dynamic systems. Automatica 2009;45:1965–9.

[47] Yang J, Li S, Yu X. Sliding-mode control for systems with mismatched uncertainties via a disturbance observer. IEEE Trans Ind Electron 2013;60:160–9.

[48] Dadra S, Momeni HR. Fractional sliding mode observer design for a class of uncertain fractional order nonlinear systems. In: Proc. of IEEE Conf. on Decision and Control and European Control Conference; 2011. p. 6925–30.

[49] Tan Y, Muttaqi KM, Meegahapola L, Ciufo P. Deadband control of doubly-fed induction generator around synchronous speed. IEEE Trans Ener Conv 2016;31(4):1610–21.

[50] Morshed MJ, Fekih A. A comparison study between two sliding mode-based controls for voltage sag mitigation in grid connected wind turbines. In: Proc. of IEEE Conf. on Cont. App.; 2015. p. 1913–8.

[51] Ullah N, Farooq Z, Zaman T, Sami I, Ibeas A, Techato K, et al. A computationally efficient robust voltage control for a single phase dual active bridge. Energy Rep 2020;6:3346–56.

[52] Musarrat MN, Islam MR, Muttaqi KM, Sutanto D. Minimization of the Thermal Stress on the Rotor Side Converter of DFIG while Operating Around Synchronous Speed. In: Proc. of IEEE Int. Conf. Power Elect, Drives and Ener. Syst. (PEDES), Chennai, India; 2018. p. 8707709.